FERMILAB-PUB-08-523-APC

# Beam physics of the 8-GeV H-minus linac

J.-P. Carneiro*

*Fermi National Accelerator Laboratory, Batavia, Illinois 60510 USA*

B. Mustapha, P. N. Ostroumov

*Argonne National Laboratory, Argonne, Illinois 60439 USA*

**Abstract**

Fermilab is developing the concept and design of an 8-GeV superconducting H-minus linac with the primary mission of increasing the intensity of the Main Injector for the production of neutrino superbeams. The front-end of the linac up to 420 MeV operates at 325 MHz and accelerates the beam from the ion source using a room temperature radio-frequency quadrupole followed by short CH type resonators and superconducting spoke resonators. In the high energy section, the acceleration is provided by superconducting elliptical 1.3 GHz cavities similar to the ones developed for the International Linear Collider (ILC). The beam physics for the linac is presented in this paper using two beam dynamics codes: `TRACK` and `ASTRA`.

*Key words:* Accelerator modeling, hydrogen ion linac.

## 1. Introduction

The development of superconducting cavities for low and medium beta proton and ion acceleration gave rise in the recent years to several proposals for high intensity proton accelerators based on superconducting technology [1]. These proton drivers can deliver up to multi-MW beams in either CW or pulsed mode (<100 MHz) and are being developed for applications such as spallation neutron sources, production of radioactive ion beams, transmutation of nuclear waste or neutrino physics.

*Corresponding author

*Email address:* `carneiro@fnal.gov` (J.-P. Carneiro)

The proposed FNAL Proton Driver is an 8-GeV superconducting $H^-$ linac conceived with the primary mission of increasing the intensity of the FNAL Main Injector. Observation of CP violation, measurement of the neutrino mass-squared differences and general understanding of neutrino properties are goals of the U.S. neutrino program the accelerator is designed to address. There are many other possible applications such as fixed target programs or acceleration of other species ($e^-$, p, $\mu$, etc...) as discussed in References [2] and [3]. This paper presents the beam dynamics of the FNAL Proton Driver performed with the simulation codes `TRACK` [4] and `ASTRA` [5]. Developed by Argonne National Laboratory to fulfill the requirement of heavy-ion linacs, `TRACK` is the primary tool in the design of the accelerator. `ASTRA`, developed by the Deutsches Elektronen-Synchrotron laboratory (Hamburg, Germany), is mainly used for the design of electron photoinjectors and we present for the first time the application of this code for hydrogen ion linacs.

## 2. Layout of the linac

The FNAL 8 GeV linac is designed to deliver $1.56{\cdot}10^{14}$ protons to the Main Injector in typical pulse lengths of 1 msec leading to an average beam current of 25 mA per pulse. At a kinetic energy of 8 GeV and a repetition rate of 10 Hz the corresponding beam average power is ∼2 MW. Based on the design published in 2006 [6], the proposed linac has the characteristics listed in Table 1.

Table 1: Basic parameters of the FNAL 8 GeV Superconducting Linac.

| Beam parameter | Value | Unit |
|---|---|---|
| Particle type (baseline mission) | $H^-$ | |
| Beam kinetic energy | 8 | GeV |
| Beam current (averaged over the pulse) | 25 | mA |
| Pulse repetition rate | 10 | Hz |
| Pulse length | 1 | msec |
| Linac RF duty cycle | 1 | % |
| Number of protons per pulse | $1.56 \cdot 10^{14}$ | |
| Beam pulsed power | 200 | MW |
| Beam averaged power | 2 | MW |
| Average RF power (estimate) | 12.5 | MW |

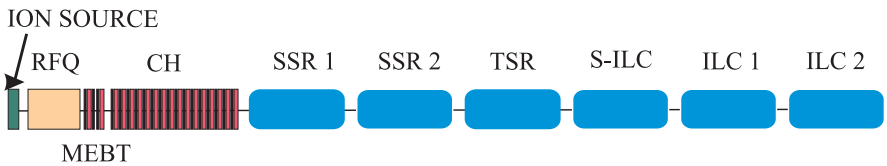


Figure 1: Schematic layout of the FNAL 8-GeV Superconducting Linac.

A schematic layout of the FNAL 8 GeV linac is presented in Figure 1. The $H^-$ beam from the Ion Source is bunched and accelerated to 2.5 MeV by a Radio-Frequency Quadrupole operating at 325 MHz. The input and output beam parameters from the RFQ are presented in Section 5 for the nominal operating current of the FNAL 8 GeV linac. Downstream of the RFQ, a Medium Energy Beam Transport (MEBT) system provides the space for a fast chopper that eliminates the unwanted bunches and forms an optimal beam time structure for multi-turn charge-exchange injection into the Main Injector with minimum uncontrolled beam losses. This chopping decreases the beam average current over the 1 msec pulse from ∼45 mA to ∼25 mA.

Typical front-end designs for proton drivers are made of normal-conducting structures (like Drift Tube Linacs and Coupled Cavity Linacs) with a transition to superconducting structures at high-energy: 160 MeV for the CERN Superconducting Proton Linac (SPL, [7]), 185 MeV for the Spallation Neutron Source (SNS, [8]) or 400 MeV for the Japan Proton Accelerator Research Complex linac (J-PARC, [9]). A different approach has been taken in the design of the FNAL 8 GeV linac. Taking advantage of the development and excellent performance of Spoke cavities ([10], [11]), it was decided to accelerate the beam from ∼10 MeV to ∼420 MeV with two types of superconducting Single Spoke Resonators (SSR 1 and SSR 2) and one type of superconducting Triple Spoke Resonators (TSR). The Spoke cavities not only present the advantage of higher accelerating gradient and cost-effective operation but also allow one single klystron to power several cavities with the use of high-power ferrite vector modulators [12]. With this outstanding feature of the FNAL 8 GeV linac, only five J-PARC type 2.5 MW klystrons are necessary to power the entire 420-MeV front-end of the linac. To boost the beam from 2.5 MeV to 10 MeV it was decided to use 16 room temperature cross-bar H-type (CH) cavities which have a higher shunt impedance (60 to 90 MOhm/m) than Drift Tube Linacs. Cavities of this type have been

Table 2: Main linac parameters with focusing type for each section (S: Solenoid, R: Resonator, nR: n Resonators, F: Focusing quad, D: Defocusing quad and $L_f$: Period Length).

| Section | $W_{out}$ (MeV) | Cavities No. | Focusing Type | Period No. | $L_f$ (m) | $z$ (m) |
|---|---|---|---|---|---|---|
| RFQ | 2.5 | 1 | - | - | - | 4 |
| MEBT | 2.5 | 2 | S1R | - | - | 6.65 |
| CH | 10 | 16 | S1R | 16 | 0.49-0.75 | 17 |
| SSR1 | 32 | 18 | S1R | 18 | 0.75 | 31.4 |
| SSR2 | 124 | 33 | S2R | 18 | 1.6 | 61.0 |
| TSR | 421 | 42 | FRDR | 21 | 3.8 | 142.2 |
| S-ILC | 1223 | 56 | F2RD2R | 14 | 6.1 | 226.7 |
| ILC1 | 2445 | 63 | F4RD3R | 9 | 12.2 | 336.5 |
| ILC2 | 8000 | 224 | F8RD8R | 14 | 24.4 | 678.1 |
| Total | | 455 | | 110 | | ∼678.1 |

developed by Frankfurt University [13] as an accelerating structure for the future GSI proton injector. For this energy range, superconducting cavities are not an option as time-consuming and expensive development of several types of them would be required. Furthermore, the number of lattice transitions in the linac directly corresponds to the number of cavity types and must be minimized. Final acceleration to 8 GeV is provided by Squeezed ILC (S-ILC, $\beta_G = 0.81$) and ILC ($\beta_G = 1.0$) 1.3 GHz cavities. In fact, for this energy range, Spoke cavities become less efficient. Noteworthy the frequency transition at high-energy (∼420 MeV) is favorable to the longitudinal beam dynamics [6].

Superconducting solenoids have been selected as the focusing elements for the front-end between the RFQ and TSR sections. As discussed in [14], several advantages arise from the use of superconducting solenoids compared to the standard quadrupole focusing. For example solenoids shorten the length of the focusing period (by a factor of 2 compared to FODO focusing) which facilitates the use of the higher accelerating gradients offered by the superconducting cavities. Also solenoids are less sensitive to misalignment errors or beam mismatches and mitigate the formation of halo by providing an axial-symmetric focusing. Above ∼100 MeV, focusing is provided by FODO quadrupoles since focusing with ∼6 T solenoids can result in stripping of

the $H^-$ beam. The different sections of the linac with the corresponding main parameters are presented in Table 2. The linac is made of 110 focusing periods with lengths varying from 49 cm to 24.2 m. The beam is transferred from the linac to the Main Injector by a ∼1 km high energy transport line [15].

## 3. Lattice design

### *3.1. Design requirements for high-intensity proton linacs*

The design of the FNAL Proton Driver has been performed following the general design requirements for a high intensity proton linac in order to to avoid RMS emittance growth along the linac [16]:

- The zero current phase advance of transverse and longitudinal oscillations should be kept below 90° per focusing period to avoid parametrically-excited instabilities at high current [17].

- The transverse and longitudinal wavenumbers $k_{T0}$, $k_{L0}$ must change adiabatically along the linac. This feature minimizes the potential for mismatches and helps assure a current independent lattice. The wavenumbers of particle oscillations are expressed as [18]:

$$k_{T0} = \frac{\sigma_{T0}}{L_f}, \quad k_{L0} = \frac{\sigma_{L0}}{L_f} \tag{1}$$

  where $\sigma_{T0}$ and $\sigma_{L0}$ are the zero current transverse and longitudinal phase advances per focusing period of length $L_f$.

- Avoid the $n = 1$ parametric resonance between the transverse and longitudinal motion. The condition for occurrence of an n-th order transverse motion parametric resonance is [19]:

$$\sigma_{T0} = \frac{n}{2}\sigma_{L0} \tag{2}$$

  The strongest resonance is for $n = 1$ and can occur particularly in superconducting linacs due to the availability of high accelerating gradients and relatively long focusing periods. These instabilities can be avoided by proper choice of operational tunes in the Kapchinskiy diagram [20].

- Avoid energy exchange between the transverse and longitudinal planes via space-charge resonances, either by providing beam equipartitioning [21] or by avoiding instable areas in Hofmann's stability charts [22].

- Provide proper matching in the lattice transitions to avoid appreciable halo formation [23].

All the above requirements need to be taken into account in the design of the linac, especially in its front end, in order to control the growth of beam halo that would lead to particle losses and radio-activation of beam line components.

*3.2. Loss assessment and $H^-$ stripping limitations*

The most challenging requirement in the design of a high power $H^-$ linac is to minimize beam loss and be able to perform timely "hands-on maintenance" on the accelerator when needed. This requirement implies an activation limit below 100 mrem/hr at 30 cm from the component surface, after extended operation of the machine ($\sim$100 days) and four hours of down time [24]. Simulations and measurements for operating facilities such as the Los Alamos Neutron Science Center (LANSCE) 800 MeV proton and $H^-$ linac and Proton Accumulator Ring indicate this criterion corresponds to a beam power loss of about 1 W/m or less [25]. Figure 2 shows the permissible beam loss per unit length to achieve 1 W/m as a function of the beam kinetic energy along the FNAL 8 GeV linac. At the final beam energy, losses should not exceed $5 \times 10^{-7}$ m$^{-1}$ for linac operation at 2 MW.

Beam losses along the accelerator can be divided into two categories: controlled beam losses which occur at a beam chopper, a collimator, or a beam dump and uncontrolled beam losses arising from misalignment of accelerator components, RF phase and amplitude jitter in the accelerating cavities, beam halo formation, etc. In a high power $H^-$ linac, another source of uncontrolled beam loss is the stripping of the $H^-$ ions. In fact, $H^-$ ions are rather delicate, having an electron affinity of only 0.75 eV. As the ions travel through the linac, they are subject to blackbody radiation, electromagnetic fields, and collisions with residual gas molecules. Any one of these three effects may strip the loosely bound electron resulting in a neutral hydrogen ion. Because the neutral atom is no longer affected by the accelerating and focusing elements, it will generally produce uncontrolled beam loss. A detailed study of these three stripping mechanisms is presented in Reference [26]. In the

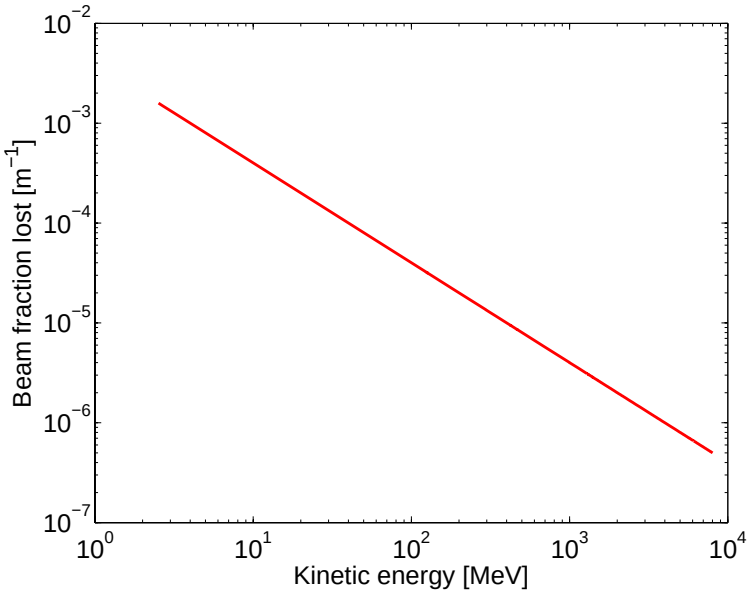


Figure 2: Permissible beam loss fraction as a funtion of the beam kinetic energy to achieve 1 W/m for the FNAL 8 GeV linac operating at 2 MW.

design of the FNAL 8 GeV linac, a particular attention has been taken to avoid $H^-$ stripping in the transverse magnetic field produced by the focusing elements. In fact, the electric fields resulting from the Lorentz transformation of the magnetic field into the beam rest frame can become large enough to effectively strip the $H^-$ beam. Figure 3 gives an estimate of the permissible maximum transverse magnetic field as a function of the beam energy along the FNAL 8 GeV linac to keep stripping losses from magnetic elements below 0.1 W/m. The beam fraction lost per unit length presented in this figure is defined as :

$$\frac{1}{L} = \frac{1}{\beta c \gamma \tau_0} \tag{3}$$

where $\tau_0$ is the ion lifetime in its rest-frame, $\beta$ is the particle relative velocity, $c$ is the speed of light and $\gamma$ is the Lorentz factor. The rest-frame lifetime $\tau_0$ for single electron detachment of an $H^-$ ion subjected to an electric field is given by Scherk [27] and Keating [28] as

$$\tau_0 = \frac{A}{E} \exp\left(\frac{C}{E}\right) \tag{4}$$

where $A = 3.073 \cdot 10^{-6}$ V·s/m, $C = 44.14 \cdot 10^{8}$ V/m, $E = \beta\gamma c B$ is the

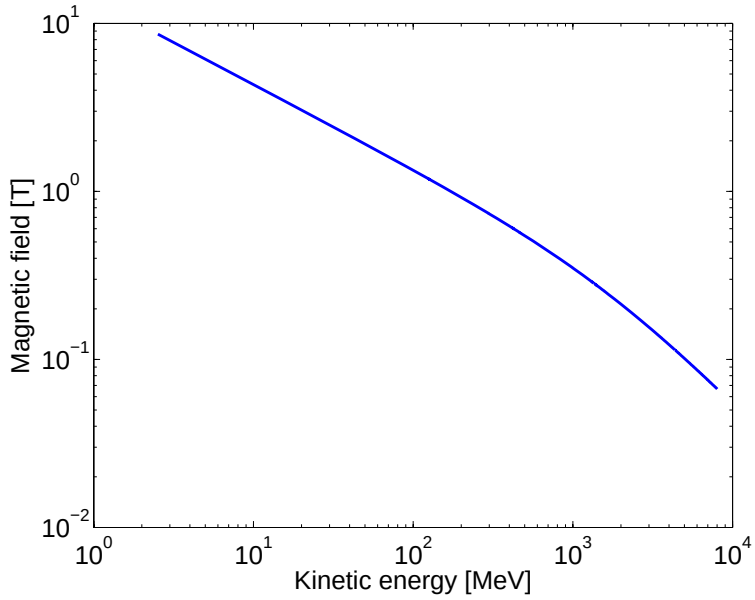


Figure 3: Permissible transverse magnetic field as a function of the beam kinetic energy to limit the beam loss from magnetic field to 0.1 W/m for the FNAL 8 GeV linac operating at its full power.

transverse electric field in the ion rest frame and $B$ is the transverse magnetic field. At the final energy of 8 GeV, Figure 3 indicates that the transverse magnetic field experienced by the beam should not exceed $\sim 6 \times 10^{-1}$ T in order to keep the stripping losses below 0.1 W/m.

## 4. Code description

### *4.1. Integration of the equations of motion*

The equations of motion for a particle in an electromagnetic field are:

$$\frac{d\vec{r}}{dt} = \frac{\vec{p}}{m_0\gamma} \tag{5}$$

$$\frac{d\vec{p}}{dt} = q(\vec{E} + \frac{\vec{p}}{m_0\gamma} \times \vec{B}) \tag{6}$$

where $\vec{r}$ is the particle coordinate, $\vec{p}$ is the momentum, $\gamma$ is the Lorentz factor, $q$ and $m_0$ are the charge and rest mass of the accelerated particle,

$\vec{E}$ and $\vec{B}$ are the electric and magnetic fields. The codes TRACK [4] and ASTRA [5] perform the integration of Equations (5) and (6) by the Runge-Kutta method of fourth order, with a variable integration step size. TRACK uses a spatial integration step defined for each element of the beam line while ASTRA uses a user defined temporal integration step. The $\vec{E}$ and $\vec{B}$ fields include external contributions from accelerating and focusing fields and internal contributions from the beam space-charge forces. Both codes have the ability of using 3D external electric fields defined on a rectangular mesh. Concerning the external solenoid magnetic fields, TRACK handles 3D fields while ASTRA supports only 1D input fields defined on the axis and used inside the code for a $3^{rd}$ order expansion as follow:

$$B_z(z,r) = B_z(z,0) - \frac{r^2}{4}\left(\frac{d^2B}{dz^2} - \frac{d^4B}{dz^4}\frac{r^2}{16} + \frac{d^6B}{dz^6}\frac{r^4}{576}\right) \quad (7)$$

$$B_r(z,r) = -\frac{r}{2}\left(\frac{dB}{dz} - \frac{d^3B}{dz^3}\frac{r^2}{8} + \frac{d^5B}{dz^5}\frac{r^4}{192}\right) \quad (8)$$

with $B_{z,0}$ the longitudinal on-axis magnetic field.

Both codes handle 3D space-charge calculation. The space-charge fields are calculated in the beam rest frame via Poisson's equation:

$$\nabla^2\phi(r,\theta,z) = -\frac{\rho(r,\theta,z)}{\epsilon_0} \quad (9)$$

where $\phi$ is the electrostatic potential, $\rho$ is the charge density and $\epsilon_0$ is the dielectric constant. The fields are then Lorentz transformed back into the laboratory frame. A 3D Cartesian grid is used for both codes with the calculation of the electrostatic potential at each grid point. On the boundaries, TRACK considers ideal parallel conducting walls transversely and free-space longitudinally while ASTRA solves Poisson's equation in free-space. Finally, it is important to notice that, unlike TRACK, the code ASTRA does not handle the RFQ beam dynamics. Therefore, the code benchmarking starts at the exit of this element.

*4.2. Output parameters*

The RMS normalized transverse emittance is defined in this document by the relation:

$$\epsilon_u = \beta\gamma\sqrt{\langle u^2\rangle\langle (u')^2\rangle - \langle uu'\rangle^2}; \quad (10)$$

where $\beta$ is the particle relative velocity, $\gamma$ is the Lorentz factor, $u$ and $u'$ are the transverse coordinate and divergence of $x$ or $y$, and $\langle\rangle$ means an RMS value. In the longitudinal plane, the RMS normalized emittance takes the form:

$$\epsilon_z = \frac{1}{m_0 c^2}\sqrt{\langle(\delta z)^2\rangle\langle(\delta p_z)^2\rangle - \langle\delta_z \delta p_z\rangle^2}; \tag{11}$$

where $m_0c^2$ is the particle rest mass, $\delta z$ and $\delta p_z$ are the difference of the particle coordinates from the beam's average position and momentum. Concerning the total emittance, this quantity is defined in this paper as the area of the ellipse in the transverse and longitudinal phase space containing the desired fraction of the beam. The ellipse orientation is defined by the RMS parameters of the particle distribution and the total emittance is calculated by varying the half-axes until the desired fraction of the beam is enclosed in the ellipse. Finally, it is important to point out that some beam parameters (namely the maximum beam envelope, the maximum bunch length and the total emittance) are not naturally provided by `ASTRA` and are reported in this papers as computed at the exit of each one of the 110 sections.

## 5. RFQ beam dynamics

The RFQ of the FNAL 8 GeV linac has been designed to operate at a frequency of 325 MHz, it accelerates and bunches the beam from 50 keV to 2.5 MeV at the nominal current of ∼45 mA. The design of the RFQ has been performed with `TRACK` and is reported in detail in Reference [29]. The current limit of the RFQ is estimated to be around 140 mA.

One original point in the design of the RFQ is the use of an input and output radial matcher to produce axially-symmetric beam. Particular attention was paid to preserve the transverse emittance and to minimize the longitudinal emittance growth while maximizing the beam transmission and the accelerating rate. Table 3 summarizes the main RFQ parameters for the nominal input current of 45 mA. The `TRACK` simulations are executed starting with a 4-D Waterbag distribution at the RFQ entrance. The beam is tracked through the ∼3 meters long RFQ which consists of 269 accelerating cells. The DC beam is bunched in a strong non-linear external electric field and the beam's space charge field. The transverse emittance is limited by the acceptance of the RFQ and does not present any growth as reported in Table 3. The longitudinal phase space does not have such a natural boundary.

Table 3: Input and output RFQ nominal parameters. From TRACK.

| Beam parameter | | Input | Output | Unit |
|---|---|---|---|---|
| Current | $I$ | 45 | 43.25 | mA |
| Beam kinetic energy | $W$ | 0.050 | 2.5 | MeV |
| RMS norm. emittance | $\epsilon_{x,n}/\epsilon_{y,n}$ | 0.25/0.25 | 0.25/0.25 | mm-mrad |
| | $\epsilon_{z,n}$ | - | 0.37 | mm-mrad |
| | $\epsilon_{z,n}$ | - | 134 | keV-deg |
| Total emittance (100%) | $\epsilon_x/\epsilon_y$ | 1.5/1.5 | 2.4/2.4 | $\pi$ mm-mrad |
| | $\epsilon_z$ | - | 3625 | $\pi$ keV-deg |
| RMS energy spread | $\sigma_E$ | - | 18 | keV |
| RMS beam size | $\sigma_x/\sigma_y$ | 1.6/1.6 | 0.73/0.73 | mm |
| RMS bunch length | $\sigma_z$ | 2.75 | 2 | mm |

The RMS and total longitudinal emittance at the exit of the RFQ operating at its nominal current are respectively 134 keV-deg and $\sim$3625 $\pi$ keV-deg. As discussed in Section 4.2, the total emittance is defined as the area of the ellipse containing 100% of the beam. Reference [14] reports that the transverse and longitudinal phase space is approximately Gaussian at the exit of the RFQ.

## 6. Benchmarking of a static distribution

In order to examine the quality of the 3D space-charge routine in TRACK and ASTRA, a comparison of the space-charge electric fields provided by both codes on the transverse and longitudinal axis of a static distribution has been performed. This benchmarking is presented in Figure 4 for a 43.25 mA distribution of $2{\cdot}10^5$ particles generated by the code TRACK at the exit of the RFQ.

As shown in Figure 4, the codes present an excellent agreement in the computation of the space-charge electric fields. The calculation is based on a 3D equidistant Cartesian grid using the maximum number of mesh points available in the codes: $129{\times}129{\times}257$ mesh points in TRACK and $129{\times}129{\times}129$ in ASTRA. The image charge of the beam on the conducting wall computed by TRACK does not impact the field calculation for this particular distribution and this effect is negligible along the linac (except for strongly misaligned beam). This result confirms the excellent agreement between the analytical

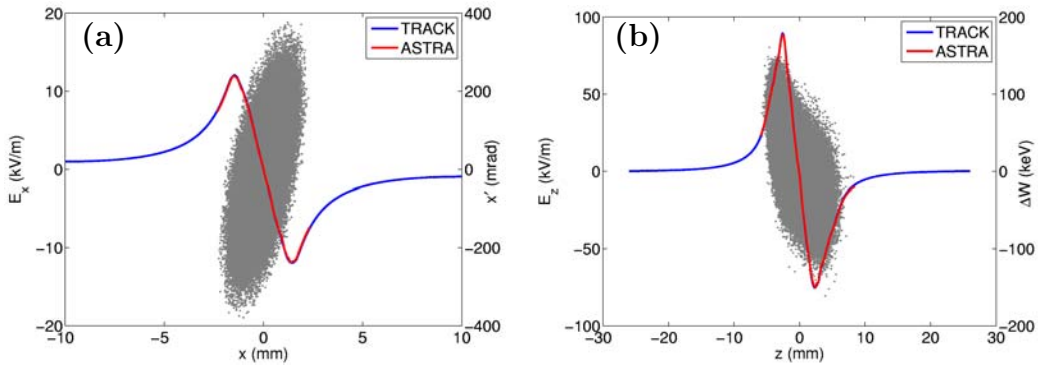


Figure 4: (a) Horizontal and (b) Longitudinal phase space of a 43.25 mA beam distribution with corresponding space-charge electric fields on axis from `TRACK` and `ASTRA`.

space-charge fields of a 3D uniform ellipsoid with those from `TRACK` and `ASTRA` previously observed and reported in [30].

## 7. Linac beam dynamics

### *7.1. Tracking at zero current*

Simulations with `TRACK` and `ASTRA` of the FNAL Proton Driver at zero current are presented in Figure 5. The transverse and longitudinal phase advances per focusing periods ($\sigma_{T0}$, $\sigma_{L0}$) depicted in Figure 5(a) present some strong but innocuous jumps due to the changing length of the focusing periods at transitions between different types of cavities. Aside from few periods the transverse and longitudinal phase advances are kept below 90°. The smooth evolution of the transverse and longitudinal wavenumbers defined in Equation 1 ($k_{T0}$, $k_{L0}$) are shown in Figure 5(b). This design requirement is achieved by properly selecting the length of the focusing periods (listed in Tab. 2) and adequately adjusting the synchronous phase of each cavity.

The Kapchinskiy diagram presented in Figure 6 shows the evolution of $\cos(\sigma_{T0})$ as a function of the defocusing factor $\gamma_s$ for each one of the 110 periods of the linac. The defocusing factor is defined as:

$$\gamma_s = \frac{\pi}{2}\frac{1}{(\beta\gamma)^3}\frac{L_f^2}{\lambda}\frac{eE_m \sin(\phi_s)}{m_0 c^2} \tag{12}$$

where $m_0c^2$ is the particle rest mass, $\beta$ is the particle relative velocity, $\gamma$ is the Lorentz factor, $\lambda$ is the wavelength of the RF field, $L_f$ is the length

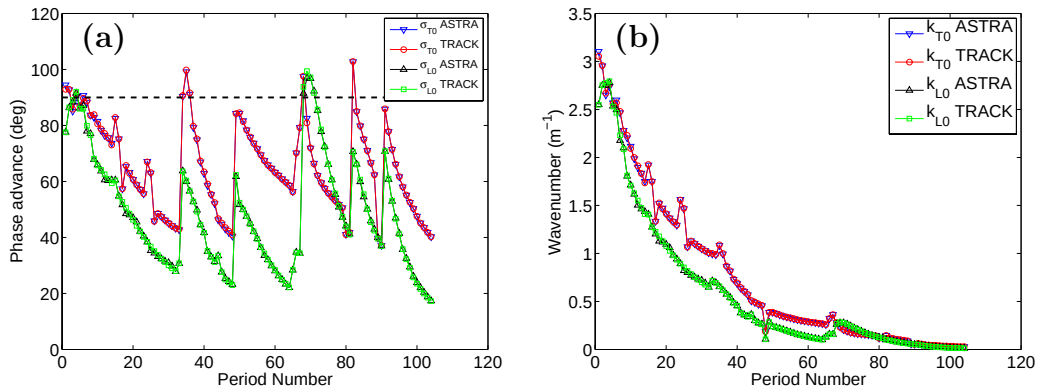


Figure 5: Zero current transverse and longitudinal (a) Phase advance and (b) Wavenumber per linac focusing period, from `TRACK` and `ASTRA`.

of the focusing period, $E_m$ is the amplitude of the equivalent traveling wave of the accelerating field and $\phi_s$ is the synchronous phase. The gray area in Figure 6 shows the boundary for the $n = 1$ parametric resonance (as defined in Eq. 2) to occur. The dashed line corresponds to the stable region for the phase motion near the separatrix boundary at a phase angle of -2$|\phi_s|$. The Kapchinskiy diagram requires the defocusing factor $\gamma_s$ to be kept below $\sim$0.7 to insure the stability for all particles. As depicted in Figure 6, the majority of the operating tunes are located in stable regions with few points lying on unstable ones. These tune points correspond to matching sections and are not expected to affect the beam since the susceptibility to instability exists for only a short distance compared to the betatron oscillation wavelength.

### *7.2. Tune depression*

An important parameter to monitor in the design of a high intensity accelerator is the tune depression $\eta$ defined as:

$$\eta = \frac{k}{k_0} \tag{13}$$

where $k$ is the wavenumber per focusing period depressed by the space-charge and $k_0$ the same parameter without space-charge. The tune depression evaluates the importance of the space-charge force in the focusing channel. In fact, high intensity beams in linacs are subject to tune depression which even if it's modest ($0.5 < k/k_0 < 1.0$) still provide a large spread of individual particles tunes which is likely to induce parametric resonances ([31], [32]).

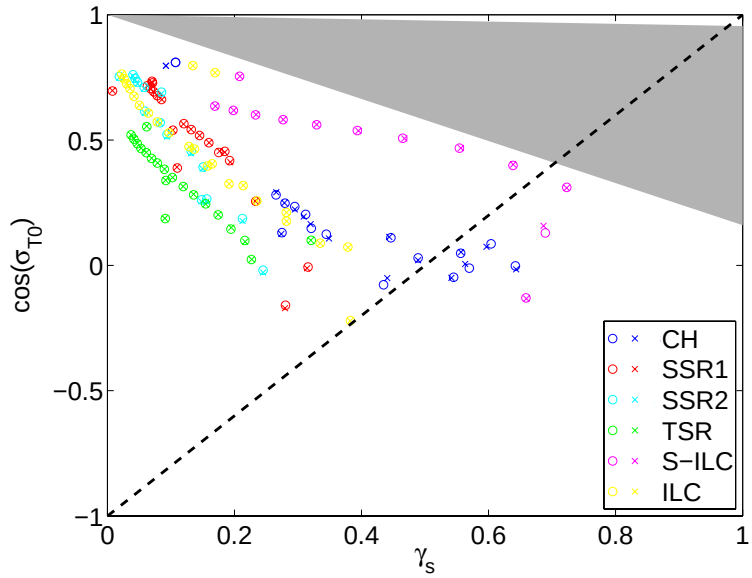


Figure 6: Kapchinskiy stability diagram. Circles represent `TRACK` and crosses `ASTRA`.

The dominant parametric resonance is the 2:1 which is caused by envelope mismatch and it is the main mechanism of halo formation.

The transverse and longitudinal tune depression computed with `TRACK` and `ASTRA` for each section of the FNAL Proton Driver at the design current of 43.25 mA is presented in Figure 7. The tune depression displayed in Figure 7 has been computed following the general equation described in Reference [25] and reported here for the ease of use which in the transverse plane takes the form:

$$\eta_T^2 = 1 - \frac{3qI\lambda(1-f)}{4\pi\epsilon_0 m_0 c^3 \gamma^3 \beta^2 (r_x + r_y) r_x r_z} \left(\frac{1}{k_{T0}}\right)^2 \tag{14}$$

and in the longitudinal one:

$$\eta_L^2 = 1 - \frac{3qI\lambda f}{4\pi\epsilon_0 m_0 c^3 \gamma^3 \beta^2 (r_x r_y r_z)} \left(\frac{1}{k_{L0}}\right)^2 \tag{15}$$

where $I$ is the average current over an RF period, $r_x$, $r_y$ and $r_z$ are the semiaxis of the equivalent ellipse over the focusing period length related to the RMS beam sizes $\sigma_i$ by $r_i = \sqrt{5} \cdot \sigma_i$, $i = x, y, z$, $f$ is the corresponding ellipsoid form factor and all other parameters being previously defined. The

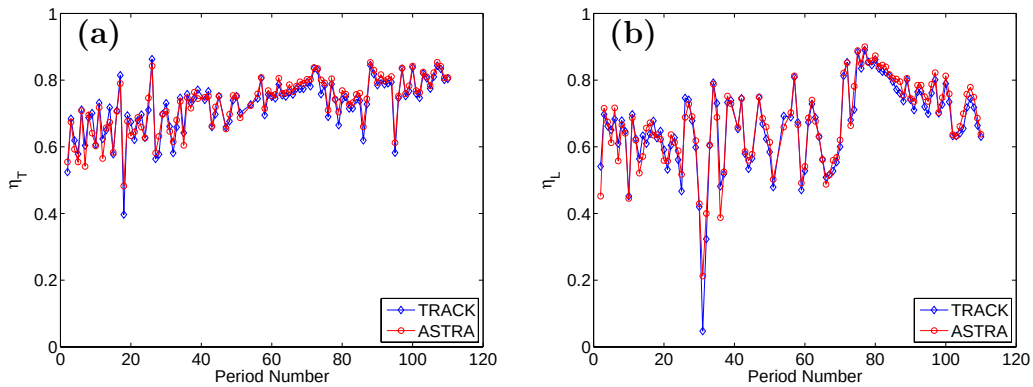


Figure 7: (a) Transverse and (b) Longitudinal tune depression per linac focusing period for a current of 43.25 mA, from `TRACK` and `ASTRA`.

simulations presented in Figure 7 predict a moderate transverse and longitudinal tune depression along the linac ($0.5 < \eta_{T,L} < 0.8$). Some points in both transverse and longitudinal planes do present stronger but inoffensive tune depression ($< 0.5$) due to matching between the different sections of the linac.

The tune depression is not only a useful tool to quantify the parametric resonances between single particles and the core of the beam, it also gives information about the coherent resonances of the core of the beam with itself called the core-core resonances. While the former resonances are related to halo formation the later are related to issue of equipartition [33]. In fact, collective space-charge density oscillations of the beam creates non-linear forces which can lead to emittance exchange between the transverse and longitudinal planes. This effect known as equipartitioning does occur if the beam presents certain combinations of anisotropy, tune-depression and tune ratio [16]. A commonly used tool in the study of core-core resonances is the Hofmann's chart which indicates, for a given longitudinal to transverse emittance ratio, regions sufficiently large to ensure stable operation of non-equipartitioned beams. Figure 8 presents the Hofmann's stability chart for a longitudinal to transverse emittance ratio of $\epsilon_L/\epsilon_T = 2$ which characterizes the FNAL Proton Driver at the design current of 43.25 mA. The horizontal axis on the chart is the ratio between the transverse and longitudinal tune depression and the vertical axis is the tune depression. The shaded areas indicate regions where non-equipartitioned beams are subject to space-charge coupling resonances that are expected to cause emittance transfer between

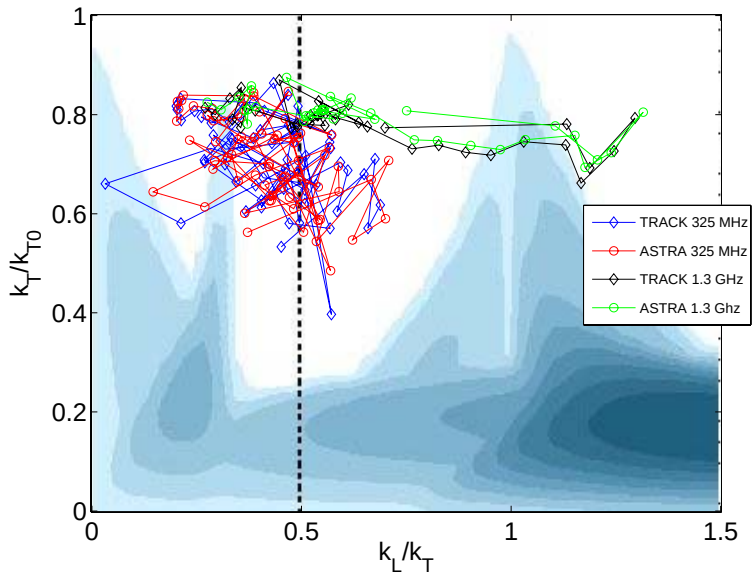


Figure 8: Hofmann stability chart for a longitudinal to transverse emittance ratio of $\epsilon_L/\epsilon_T = 2$ and a linac design current of 43.25 mA. Tunes are from `TRACK` and `ASTRA`.

transverse and longitudinal planes (the degree of shading indicates the speed of the process). The vertical dashed line shows the condition for equipartition. The dangerous resonance in the chart is the fourth order even mode one located at around a tune ratio of 1. The peaks on the left part of the chart represent weak coupling resonances that would take a long time to develop. As observed in Figure 8 the operating tunes computed with `TRACK` and `ASTRA` lie in stable (white) areas which points out that core-core resonances are not a concern for the current design of the FNAL Proton Driver.

### *7.3. Tracking at 43.25 mA*

Tracking of the 43.25 mA distribution presented in Section 6 has been performed with `TRACK` and `ASTRA` using 3D space-charge routine and a grid of 129×129×257 and 129×129×129 mesh points respectively.

Figure 9(a) shows simulations of the RMS transverse and longitudinal emittance growth factor along the linac. The primary effect for the observed RMS emittance growth is attributed to imperfect matching between the different lattice transitions of the linac. In fact, the beam mismatch causes envelope oscillations leading to a larger but acceptable emittance growth [6]. The present matching has been achieved using the matrix-based beam optics

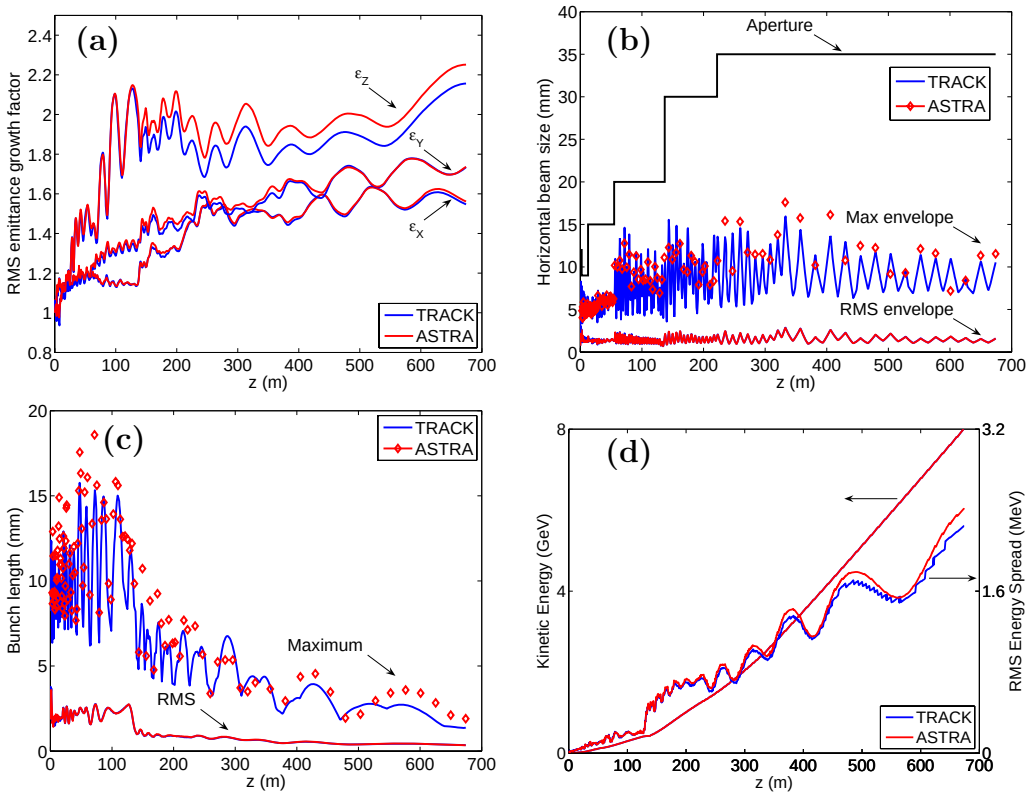


Figure 9: TRACK and ASTRA simulations of the linac at 43.25 mA, from the RFQ exit ($z = 0$ m) to the last accelerating cavity ($z \simeq 674$ m) . From top left to bottom right: (a) RMS normalized emittance, (b) RMS and Maximum beam envelope, (c) RMS and Maximum bunch length, (d) Kinetic Energy and RMS Energy Spread.

code TRACE-3D [34]. The matching should be improved in the near future using the automatic tuning procedure which is currently being implemented in TRACK. This new feature of the code, presented in Reference [35], will offer the possibility of optimizing a large number of parameters in a 3D particle code where a more realistic representation of the beam (including halo for instance) is achieved. The evolution of the RMS and maximum beam envelope and bunch length is presented in Figures 9(b) and 9(c). These simulations indicate that the maximum halo production is limited to ∼8 times its RMS value in all three phase planes, a reasonable level according to [16]. Furthermore, the use of superconducting resonators with large aperture (see Fig. 9(b)) enables the ratio between the minimum beam tube radius and

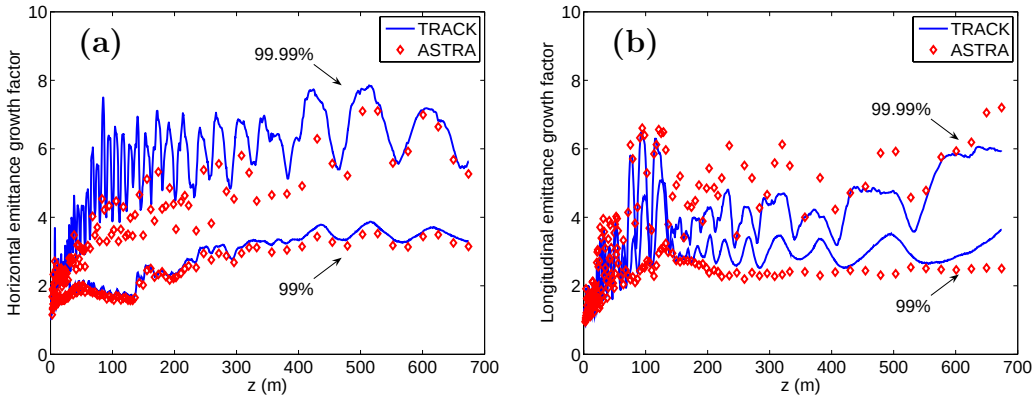


Figure 10: (a) Horizontal and (b) Longitudinal total emittance growth factor (99.99% and 99%) along the linac for a current of 43.25 mA, from `TRACK` and `ASTRA`.

the RMS beam size to stay higher than 10, a safe margin to avoid losses as discussed in [16]. The energy and energy spread along the linac is shown in Figure 9(d). Noteworthy the excellent agreement between `TRACK` and `ASTRA` depicted in Figure 9: the transverse parameters (RMS emittance and envelope) are within 1% after ∼674 meters of tracking and the longitudinal parameters (RMS bunch length, emittance, kinetic energy and RMS energy spread) are within 5%. This result is in agreement with the values observed in [36] where a detailed linac code benchmarking concerning the high current regime of the UNILAC experiment at GSI is presented and a deviation of few percent between several codes reported.

The total-to-RMS emittance ratio relates to the tail of the distribution and indicates how far particles deviate in the phase space compared to the core of the distribution [17]. This ratio is therefore a useful tool to monitor the halo formation. Figure 10 shows the evolution of the 99.99% and 99% horizontal and longitudinal total-to-RMS emittance ratio along the linac from `TRACK` and `ASTRA`. Both codes predict a fairly constant evolution of the 99% horizontal and longitudinal emittance ratio. A substantial increase of the 99.99% emittance ratio in both the horizontal and longitudinal planes is visible and can be related to the imperfect matching between the different sections of the linac as previously mentioned. For the present design of the FNAL Proton Driver at 43.25 mA, only 1% of the particles are outside $\sim 20 \cdot \epsilon_{RMS}$. This represents an acceptable level and enables the transport of the $2 \cdot 10^5$ matched beam distribution from the RFQ to the end of the linac

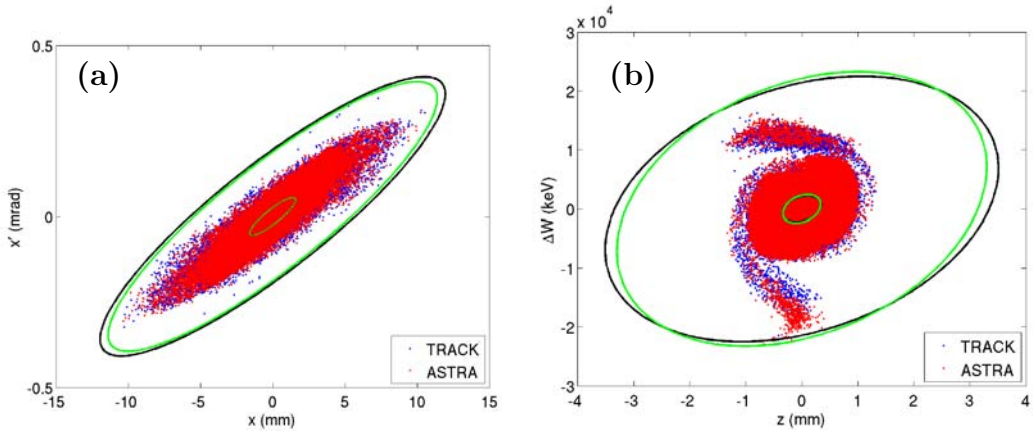


Figure 11: (a) Horizontal and (b) Longitudinal final phase space of a 43.25 mA beam distribution from `TRACK` and `ASTRA` with corresponding 99.99% and RMS beam ellipse (black ellipses for `TRACK` and green ellipses for `ASTRA`).

without any losses. The final horizontal and longitudinal phase spaces at the exit of the linac are presented in Figure 11 with the corresponding RMS and 99.99% ellipses. The overall shape of the distributions confirms the excellent behavior of the codes.

## 8. Beam losses

Typical values of element misalignment and cavity jitter (phase and field) have been implemented into `TRACK` and beam loss simulations performed from the RFQ exit to the end of the FNAL 8 GeV linac. In order to get high-statistics, 100 simulations were performed on the Fermigrid [37] with a different seed for the random number generator used in each simulation. The simulations were performed with $10^6$ macroparticles and the losses were scaled to a beam power of 2 MW. The set of misalignments and RF errors implemented into `TRACK` are reported in Table 4 and the corresponding beam power loss per meter along the linac in Figure 12(a). The misalignment errors are generated in `TRACK` with a Uniform distribution and the jitter of the cavities are generated with a Gaussian distribution (truncated at $\pm 3$ sigma RMS). It is interesting to notice in Figure 12(a) that the beam losses remain below the acceptable limit of 1 W/m (discussed in Section 3.2) except in the section of the linac where the frequency transition from 325 MHz to 1.3 GHz occurs. At this location, beam losses are slightly above 1 W/m.

Table 4: Typical values of misalignment and RF errors. The errors correspond to the maximum width of the Uniform distributions and the RMS width of the Gaussian distributions (truncated at 3 sigma).

| Component | Error value | Distribution |
|---|---|---|
| Solenoids offset ($x$ and $y$) | 0.15 mm | Uniform |
| Quadrupoles offset ($x$ and $y$) | 0.15 mm | Uniform |
| Quadrupoles rotation around the z-axis | 5 mrad | Uniform |
| CH cavities offset ($x$ and $y$) | 5 mm | Uniform |
| SC Spoke cavities offset ($x$ and $y$) | 5 mm | Uniform |
| S-ILC and ILC cavities offset ($x$ and $y$) | 1 mm | Uniform |
| Phase jitter of the cavities | 1.0° | Gaussian |
| Field jitter of the cavities | 1.0% | Gaussian |

In the simulations presented in Figure 12(a), no correction elements have been implemented in `TRACK`, therefore the beam losses represent the higher-limit scenario for the set of misalignment and RF errors of Table 4. We believe that the correction elements will keep the beam loss at the frequency transition below the 1 W/m loss criterion widely adopted by the accelerator community.

Recently, numerical simulations of $H^-$ stripping losses from blackbody radiation, electromagnetic fields, and residual gas have been implemented into `TRACK`. These studies reported in Reference [26] indicate that, for a typical operation of the FNAL 8 GeV linac (vacuum pressure of $1 \times 10^{-7}$ torr in the room-temperature sections of the linac and $1 \times 10^{-10}$ torr in the cryomodules), the stripping losses remain below 0.1 W/m for 2 MW power. These simulations are reported in Figure 12(b): the stripping losses represent a background ranging from $\sim 10^{-3}$ W/m at the start of the linac to 0.1 W/m in the high-energy section and therefore do not have a significant impact on the losses along the linac. As reported in Reference [26], the main contributor to the stripping losses are the residual gas (mainly at the start of the linac) and the blackbody radiation in warm sections between the cryomodules (preponderant in the high-energy sections), the stripping losses from the electromagnetic fields being negligible $< 10^{-3}$ W/m.

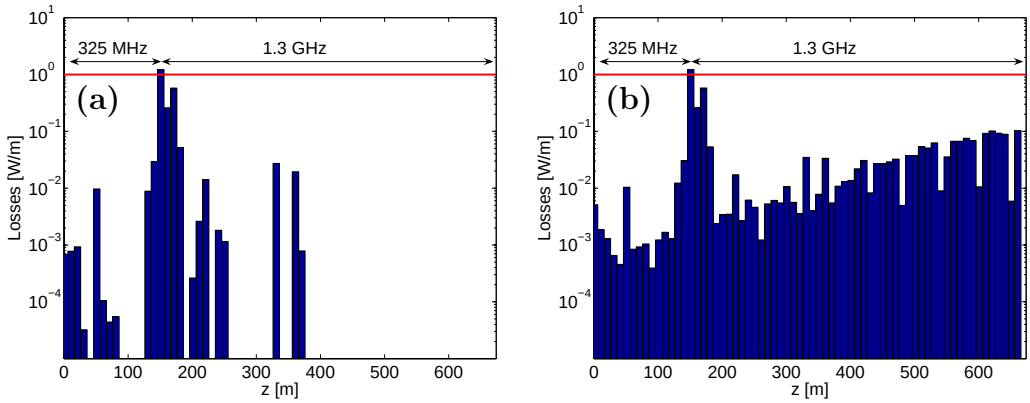


Figure 12: TRACK simulations of the beam fraction lost per meter along the FNAL 8 GeV linac operating at 2 MW for (a) the set of misalignment and RF errors presented in Table 4 and (b) including stripping losses from blackbody, residual gas and electromagnetic field. The red line indicates the 1 W/m limit.

## 9. Conclusion

A detailed beam dynamics simulation of the FNAL 8-GeV $H^-$ superconducting linac is presented in this paper from the exit of the RFQ to the last accelerating section with two codes TRACK and ASTRA. These studies confirmed the excellent behavior of the linac in terms of emittance growth and beam losses for the current design of the linac at 43.25 mA. An excellent agreement between the codes has also been observed which confirms the robustness of the design. A parallel version of TRACK, called PTRACK, is being implemented on the BG/P supercomputer at ANL [38] which will allow high statistics simulations (using up to the real number of particles in the bunch). Futher development of PTRACK will include a realistic low-level rf model [39] which will enable even more detailed beam dynamics.

## Acknowledgments

The authors would like to thank V. Aseev (ANL), D. Johnson, V. Shiltsev and R. C. Webber (FNAL) for helpful discussion and information, K. Floettmann (DESY) for his support in using ASTRA and I. Hofmann (GSI) for providing the stability chart. This work is supported by the U.S. Department of Energy under Contracts DE-AC02-06CH11357 and DE-AC02-07CH11359.

## References


[1] F. Gerigk, Future high-intensity proton accelerators, CERN-AB 2007-035, CERN, Geneva, Switzerland (Oct 2007).

[2] G. W. Foster, J. A. MacLachlan, A multi-mission 8 GeV injector linac as a Fermilab booster replacement, in: Proceedings of the International Linear Accelerator Conference, Gyeongju, Korea, 2002.

[3] An 8 GeV superconducting linac proton driver, Tech. rep. (Nov 2005). URL `http://protondriver.fnal.gov/#Technical_Design_Link`

[4] V. N. Aseev, P. N. Ostroumov, B. Mustapha, TRACK: The new beam dynamics code, in: Proceedings of the Particle Accelerator Conference, Knoxville, Tennessee, 2005.

[5] K. Floettmann, ASTRA User Manual (2002). URL `http://www.desy.de/~mpyflo/Astra_dokumentation`

[6] P. N. Ostroumov, Physics design of the 8-GeV H-minus linac, New Journal of Physics 8 (11) (2006) 281.

[7] Conceptual design of the SPL II, a high-power superconducting H- linac at CERN, Tech. rep., CERN-2006-006 (2006).

[8] A. Aleksandrov, C. Allen, S. Cousineau, V. Danilov, J. Galambos, D. Jeon, J. Holmes, T. Pelaia, M. Plum, A. Shishlo, M. Stockli, Y. Zhang, Performance of the SNS front and warm linac, in: Proceedings of the European Particle Accelerator Conference, Genoa, Italy, 2008.

[9] K. Hasegawa, Commissioning of the J-PARC linac, in: Proceedings of the Particle Accelerator Conference, Albuquerque, New Mexico, 2007.

[10] M. Kelly, Overview of TEM-class superconducting cavities for proton and ion acceleration, in: Proceedings of the International Linear Accelerator Conference, Knoxville, Tennessee, 2006.

[11] K. W. Shepard, P. N. Ostroumov, J. R. Delayen, High-energy ion linacs based on superconducting spoke cavities, prstab 6 (8) (2003) 080101.

[12] R. L. Madrak, D. Wildman, High power 325 MHz vector modulators for the Fermilab high-intensity neutrino source (HINS), in: Proceedings of the International Linear Accelerator Conference, Vancouver, British Columbia, 2008.

[13] Z. Li, R. Tiede, U. Ratzinger, H. Podlech, C. Clemente, K. Dermati, W. Barth, L. Groening, Design of the R.T. CH-cavity and perspectives for a new GSI proton linac, in: Proceedings of the International Linear Accelerator Conference, Luebeck, Germany, 2004.

[14] P. N. Ostroumov, J.-P. Carneiro, Physics design of front-ends for superconducting ions linacs, in: Proceedings of the Advanced Beam Dynamics Workshop on High-Intensity, High-Brightness Hadron Beams, Nashville, Tennessee, 2008.

[15] D. E. Johnson, P. Yoon, C.-J. Liaw, D. Raparia, J. Beebe-Wang, An 8-GeV multi-turn injection system for the Fermilab main injector, in: Proceedings of the Particle Accelerator Conference, Albuquerque, New-Mexico, 2007.

[16] F. Gerigk, Space-charge and beam halos in proton linacs, in: Proceedings of the Joint USPAS-CAS-Japan-Russia Accelerator School, Long Beach, California, 2002.

[17] M. Reiser, Theory and design of charged particle beams, John Wiley & Sons, New-York, 1994.

[18] S. Nath, K. Crandall, E. Gray, T. Wangler, L. Young, Beam dynamics aspects for the APT integrated linac, Vol. 1, 1997, pp. 1162–1164 vol.1.

[19] P. Lapostolle, M. Weiss, Formulae and procedures useful for the design of linear accelerators, CERN-PS 2000-001, CERN, Geneva, Switzerland (Jan 2000).

[20] I. M. Kapchinskiy, Theory of resonance linear accelerators, Hardwood Academic Publishers, 1985.

[21] L. M. Young, Equipartitioning in a high current proton linac, in: Proceedings of the Particle Accelerator Conference, Vancouver, Canada, 1997.

[22] I. Hofmann, Stability of anisotropic beams with space charge, Phys. Rev. E 57 (4) (1998) 4713–4724.

[23] T. P. Wangler, Beam halo in proton linac beams, in: Proceedings of the International Linear Accelerator Conference, Monterey, California, 2000.

[24] N. Catalan-Lasheras, Y. Y. Lee, H. Ludewig, D. Raparia, J. Wei, Beam Loss and Collimation at SNS Ring, in: N. V. Mohkov, W. Chou (Eds.), Beam Halo and Scraping: The 7th ICFA Mini-Workshop on High-Brightness Hadron Beams, Lake Como, Wisconsin, 1999, no. FERMILAB-Conf-00/185, FNAL, Batavia, Illinois, 2000, pp. 107–111.

[25] T. P. Wangler, E. R. Gray, F. L. Krawczyk, S. S. Kurennoy, G. P. Lawrence, R. D. Ryne, K. R. Crandall, Basis for Low Beam Loss in the High-Current APT Linac, in: C. E. Eyberger, R. C. Pardo, M. M. White (Eds.), Proceedings of the XIX International Linac Conference: Chicago, Illinois, 1998, no. ANL-98/28, ANL, Argonne, Illinois, 1998, pp. 657–659.

[26] J.-P. Carneiro, B. Mustapha, P. N. Ostroumov, Numerical simulations of stripping effects in high-intensity hydrogen ion linacs, submitted to Phys. Rev. ST Accel. Beams.

[27] L. R. Scherk, An improved value for the electron affinity of the negative hydrogen ion, Can. J. Phys. 57 (1979) 558–563.

[28] P. B. Keating, M. S. Gulley, H. C. Bryant, E. P. Mackerrow, W. A. Miller, D. C. Rislove, S. Cohen, J. B. Donahue, D. H. Fitzgerald, D. J. Funk, S. C. Frankle, R. L. Hutson, R. J. Macek, M. A. Plum, N. G. Stanciu, O. B. van Dyck, C. A. Wilkinson, Electric-field-induced electron detachment of 800-MeV $H^-$ ions, Phys. Rev. A. 52 (1995) 4547–4555.

[29] P. N. Ostroumov, V. N. Aseev, A. A. Kolomiets, Application of a new procedure for design of 325 MHz RFQ, Journal of Instrumentation 1 (04) (2006) P04002.

[30] J.-P. Carneiro, Benchmarking of simulation codes TRACK and ASTRA for the FNAL high-intensity proton source, in: Proceedings of the International Linear Accelerator Conference, Knoxville, Tennessee, 2006.

[31] T. P. Wangler, K. R. Crandall, R. Ryne, T. S. Wang, Particle-core model for transverse dynamics of beam halo, prstab 1 (8) (1998) 084201.

[32] A. V. Fedotov, Beam halo formation in high-intensity beams, NIM A 557 (2006) 216–219.

[33] I. Hofmann, G. Franchetti, J. Qiang, R. Ryne, F. Gerigk, D. Jeon, N. Pichoff, Review of beam dynamics and space charge resonances in high intensity linacs, in: Proceedings of the European Particle Accelerator Conference, Paris, France, 2002.

[34] K. R. Crandall, D. P. Rusthoi, TRACE 3-D Documentation, Los Alamos LA-UR-97-886 (1997).

[35] B. Mustapha, P. N. Ostroumov, Development of large scale optimization tools for beam tracking codes, in: Proceedings of 42nd ICFA Advanced Beam Dynamics Workshop on High-Intensity, High-Brightness Hadron Beams, Nashville, Tennessee, 2008.

[36] A. Franchi, W. Bayer, G. Franchetti, L. Groening, I. Hofmann, A. Orzhekhovskaya, S. Yaramyshev, X. Yin, Linac code benchmarking in preparation of the UNILAC experiment, CARE-NOTE 2006-011-HIPPI (2006).

[37] Fermi Grid web site.
URL `http://fermigrid.fnal.gov`

[38] J. Xu, B. Mustapha, V. N. Aseev, P. N. Ostroumov, Simulations of high-intensity beams using BG/P supercomputer at ANL, in: Proceedings of 42nd ICFA Advanced Beam Dynamics Workshop on High-Intensity, High-Brightness Hadron Beams, Nashville, Tennessee, 2008.

[39] G. Cancelo, A. Vignoni, Optimizing cavity gradients in pulsed linacs using the cavity transient response , in: Proceedings of the International Linear Accelerator Conference, Vancouver, British Columbia, 2008.